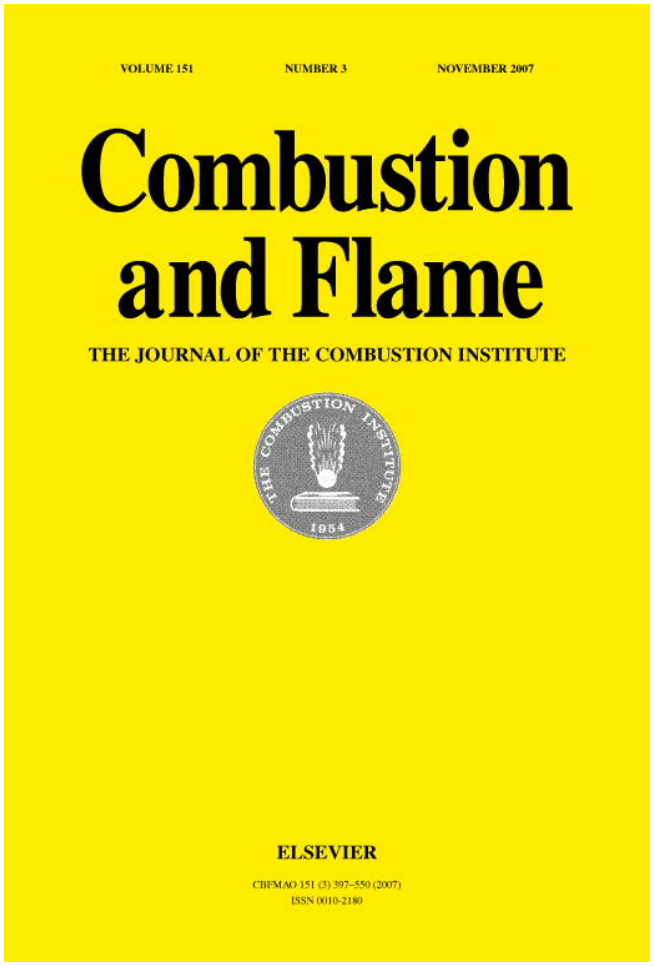

Available online at www.sciencedirect.com
ScienceDirect
Combustion and Flame 151 (2007) 495–511
Combustion and Flame
www.elsevier.com/locate/combustflame

Transport budgets in turbulent lifted flames of methane autoigniting in a vitiated co-flow

Robert L. Gordon [a,*], Assaad R. Masri [a], Stephen B. Pope [b], Graham M. Goldin [c]

[a] *School of Aerospace, Mechanical and Mechatronic Engineering, The University of Sydney, NSW 2006, Australia*
[b] *Mechanical and Aerospace Engineering Cornell University, Ithaca, NY 14853, USA*
[c] *Fluent Inc., Lebanon, NH, USA*

Received 25 May 2006; received in revised form 25 April 2007; accepted 3 July 2007

Available online 24 August 2007

Abstract

Autoignition of hydrocarbon fuels is an outstanding research problem of significant practical relevance in engines and gas turbine applications. This paper presents a numerical study of the autoignition of methane, the simplest in the hydrocarbon family. The model burner used here produces a simple, yet representative lifted jet flame issuing in a vitiated surrounding. The calculations employ a composition probability density function (PDF) approach coupled to the commercial CFD package, FLUENT. The in situ adaptive tabulation (ISAT) method is used to implement detailed chemical kinetics. An analysis of species concentrations and transport budgets of convection, turbulent diffusion, and chemical reaction terms is performed with respect to selected species at the base of the lifted turbulent flames. This analysis provides a clearer understanding of the mechanism and the dominant species that control autoignition. Calculations are also performed for test cases that clearly distinguish autoignition from premixed flame propagation, as these are the two most plausible mechanisms for flame stabilization for the turbulent lifted flames under investigation. It is revealed that a radical pool of precursors containing minor species such as CH_3, CH_2O, C_2H_2, C_2H_4, C_2H_6, HO_2, and H_2O_2 builds up prior to autoignition. The transport budgets show a clear convective–reactive balance when autoignition occurs. This is in contrast to the reactive–diffusive balance that occurs in the reaction zone of premixed flames. The buildup of a pool of radical species and the convective–reactive balance of their transport budgets are deemed to be good indicators of the occurrence of autoignition.

Keywords: Turbulent transport budgets; Nonpremixed flames; Vitiated co-flow; Autoignition; Lifted flames

1. Introduction

This paper addresses the autoignition of methane, the simplest of the hydrocarbons, and also a possible fuel for gas turbines, dual-fuel diesel engines, supersonic combustion ramjets, and HCCI engines. In some of these applications, autoignition is required to

* Corresponding author. Fax: +61 2 9351 7060.
E-mail address: r.gordon@usyd.edu.au (R.L. Gordon).

0010-2180/$ – see front matter
doi:10.1016/j.combustflame.2007.07.001

occur rapidly, while for others, designers wish to delay it to allow flame propagation into the flammable mixture [1]. Methane exhibits a relatively long ignition delay that can be reduced by the addition of higher hydrocarbons or hydrogen [2,3] and increased in to the presence of water vapor [4].

Research in this area has recently intensified, with measurements and kinetic studies of ignition delays being made over ranges of pressures and fuel mixtures in engines, combustion bombs, and shock tubes [2–6]. Numerical studies of autoignition using direct numerical simulation (DNS) for relatively simple fuels have shown that the fuel does not necessarily ignite under stoichiometric conditions, but rather at mixture fractions where the fluid is "most reactive" yet the scalar dissipation rate is relatively low and the residence times are adequate [7–10].

Intermediate in complexity between difficult measurements in real engines and expensive DNS studies is a simple laboratory-scale vitiated co-flow burner, which has been established as an excellent model problem for studying autoignition in an environment that is well controlled, yet possessing the characteristics of practical devices. The flow here is dominantly in the axial direction (with no recirculation), and the fuel jet and co-flow properties may be varied to change the liftoff height and the autoignition delay times. Recent extensive measurements in selected flames of hydrogen and methane fuels have been conducted and the data are now available on the Web [11,12].

The hybrid RANS–PDF approach has recently been used with detailed chemistry to successfully compute the structure of flames of hydrogen (both with composition PDF transport [13] and with joint velocity-turbulence frequency-composition PDF transport [14]) and methane [15] stabilized on this vitiated co-flow burner. Comparisons with available measurements are very encouraging. This implies that the confidence level in the computations of these flames is now sufficiently high so that other aspects of autoignition that are difficult to test experimentally may be studied. A greater understanding of the preignition processes may be gleaned from examining the profiles of minor species leading up to the mean flame base. Further, species transport budgets, while very difficult to measure experimentally, may be very revealing. This has been established for simple flames of hydrogen fuels where the convection, diffusion, and reaction terms are calculated and the balance of these terms is used as an indicator of the dominant stabilizing mechanism [16]. A similar approach has been adopted by de Charentenay et al. [17] using 2-D DNS of a detached laminar flame.

This approach is extended here to more complex turbulent flames of hydrocarbon fuel, which display the following different physical characteristics compared to the hydrogen/nitrogen flames: (i) the liftoff height varies linearly with co-flow temperatures, which are also higher than those used for H_2/N_2, (ii) the flames are significantly noisier, and (iii) the fluctuations in the liftoff height are large (up to 10 diameters at the greatest liftoff heights). Detailed methane chemistries are used for two flames with different co-flow temperatures and liftoff heights. Budgets for convection, diffusion, and reaction are computed at the base of these flames, as well as for two simple models representing autoignition and premixed flame propagation. The key precursors for autoignition are identified in all cases and discussed with respect to the convective–reactive balance that prevails during this process.

2. Model description

2.1. The turbulent combustion model

All computations presented here use the FLUENT 6.2 code, which solves Reynolds averaged Navier–Stokes (RANS) equations for the mean conservation of mass, momentum, and energy, together with the k–ε turbulence model using the standard constants, except for $C_{\varepsilon 1}$, which is set to 1.6 to compensate for the round-jet/plane-jet anomaly. A modeled transport equation for the composition PDF is coupled and solved using a Lagrangian particle-based Monte Carlo method. The EMST mixing model is used, with the value $C_\phi = 1.5$. The turbulent Schmidt number takes the standard value of 0.7.

The jet flame is assumed to be axisymmetric and a low-Reynolds-number turbulence model is used on the walls of the fuel tube. A steady segregated solver is used with implicit formulation. The particle Courant number is fixed at 0.5 and the underrelaxation factors for pressure, density, body forces, and momentum are set at 0.3, 1.0, 1.0, and 0.7, respectively. A second-order upwind discretization scheme is used for the momentum and turbulent kinetic energy equations, PRESTO for pressure, and PISO for pressure–velocity coupling.

The principal chemical mechanism used is ARM2 [18], an augmented reduced mechanism based on GRI2.1. It involves 19 species (H_2, H, O_2, OH, H_2O, HO_2, H_2O_2, CH_3, CH_4, CO, CO_2, CH_2O, C_2H_2, C_2H_4, C_2H_6, NH_3, NO, HCN, N_2) and 15 reactions (3 involving nitrogen species). This is incorporated into the PDF method using the in situ adaptive tabulation (ISAT) algorithm developed by Pope [19]. A comparison has been conducted with several other chemical mechanisms, detailed in Table 1. These range in complexity from the GRI2.11 mechanism

Table 1
Chemical mechanisms tested in the PDF calculations

Mechanism	No. of species[a]	No. of reactions[b]	Reference
ARM2	19 (16)	15 (12)	[18]
GRI2.11	49 (32)	277 (175)	[20]
DRM22	22	104	[21]
Skeletal	16	41	[22]
Smooke	16	46	[23,24]
5-Step	9 (8)	5 (4)	[25]

[a] In parentheses, number of H–O–C species.
[b] In parentheses, number of H–O–C reactions.

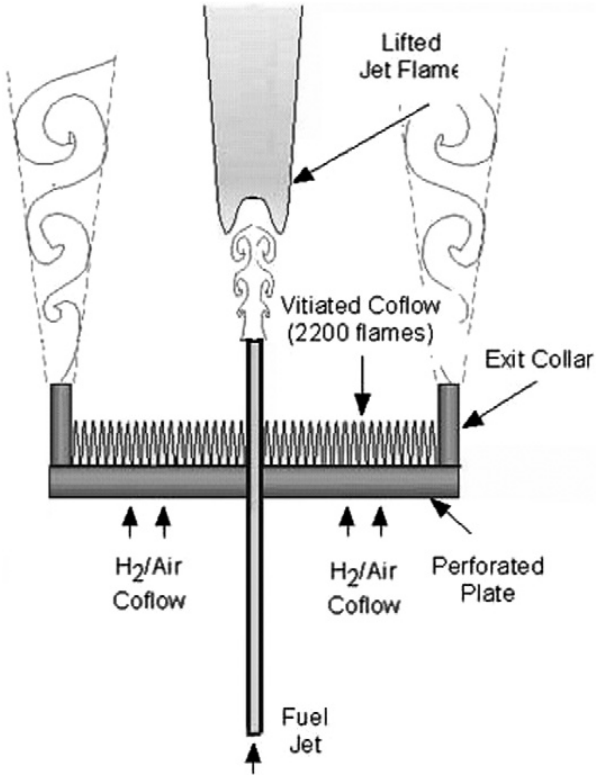

Fig. 1. Schematic of the vitiated co-flow burner.

[20], which provides the most comprehensive mechanism for methane used here, to the DRM22 mechanism [21], a skeletal mechanism as detailed by James et al. [22], the Smooke mechanism as detailed in [23] (with the three updated reactions reported in [24]), and a five-step mechanism derived from GRI2.11 [22] (hereafter referred to as 5-step).

2.2. The vitiated co-flow burner and test cases

The vitiated co-flow burner modeled in this work has been well described in earlier work [13,15,26] and is shown in Fig. 1. It consists of a fuel jet, which has an inner diameter $D = 4.57$ mm and a wall thickness of 0.89 mm, located at the center of a perforated disk with a diameter of 210 mm. The disk has 2200 holes of 1.58 mm diameter, which stabilize as many premixed flames, providing a hot co-flowing stream. The

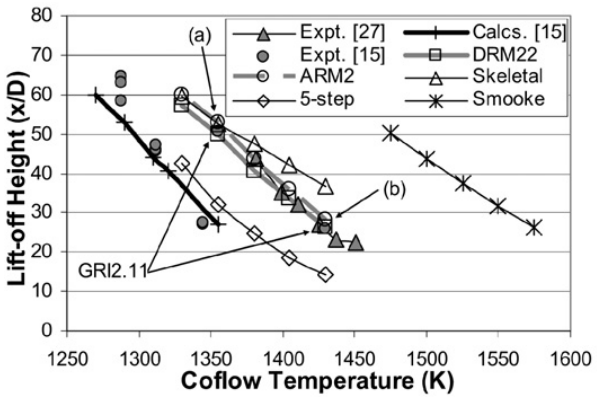

Fig. 2. Liftoff height versus co-flow temperature for six chemical mechanisms and experimental data from [27]. Previous results from [15] are plotted for comparison. The two flames investigated further are marked (a) and (b) and have co-flow temperatures of 1355 and 1430 K, respectively.

overall blockage of the perforated plate is 87%. The central fuel jet extends 70 mm downstream of the surface of the perforated plate, so that the fuel mixture exits in a co-flow of nearly uniform composition. The entire burner assembly is shrouded with a water jacket for cooling and sits in stagnant air.

The principal parameters that control the flame liftoff height characteristics in this burner are fuel jet velocity, co-flow velocity, and co-flow temperature. Although the liftoff height of the methane–air lifted flame is affected by each of these parameters [15], it exhibits the greatest sensitivity to the co-flow temperature. The liftoff height is defined, experimentally, as the average distance between the jet exit plane of the fuel pipe and the flame base where the luminescence is visible to the naked eye in a darkened room.

Fig. 2 shows a comparison of the location of liftoff height versus co-flow temperature for the current calculations relative to recent experimental and numerical investigations [15,27]. The results for the different mechanisms with respect to GRI2.11 are as expected from the investigation of Cao and Pope [24], with the Smooke mechanism displaying significantly delayed ignition times, the 5-step mechanism displaying reduced ignition delays, and the skeletal mechanism varying from reduced delays at lower temperatures to increased delays at higher temperatures, as indicated by the shallower gradient of the response curve. Both the ARM2 and DRM22 mechanisms match the GRI2.11 calculations well, and these datasets also align well with the experimental results of [27].

For the numerical results presented in Fig. 2, liftoff height has been taken as the distance to the location of the steepest axial gradient of mean OH along a path through the mean flame base (see Section 5). This is a method for determining liftoff height different from that used in [15], which was based on concentrations of C_2H_2 and C_2H_4. These species are not present

Table 2
Boundary conditions for the turbulent lifted flame case and the two test cases of counterflow premixed flame and one-dimensional autoignition channel

	Turbulent lifted flame		Opposed premixed case		Autoignition case
	Fuel jet	Co-flow	Fuel jet	Counterflow	Inlet condition
Velocity ($m\,s^{-1}$)	100	5.3	0.5	1.5	10
Temperature (K)	320	1355	320	2098.2	1251.5
k ($m^2\,s^{-2}$)	150	0.11	0.00375	0.03375	1
ε ($m^2\,s^{-3}$)	66050	5.6	0.03773	1.01881	1
Species mass fractions					
CH_4	0.21322	0	0.05107	1.68×10^{-9}	0.021429
O_2	0.18855	0.14159	0.20372	0.002017	0.146307
H_2O	0.00212	0.1013	0.07455	0.18702	0.091396
OH	0	0.000126		0.0007995	
H_2	0	7.48×10^{-6}		0.0001817	
CO				0.003689	
CO_2				0.13558	
H				3.47×10^{-6}	
NO				2.85×10^{-6}	
N_2	Balance	Balance	Balance	Balance	Balance

in the Smooke, skeletal, and 5-step mechanisms, so the OH mass fraction profiles are used in this paper for consistency between the cases. A case was run to match the conditions and models described in [15], with the remaining differences being the ARM2 mechanism and Lagrangian composition PDF transport used in this case, and the ARM1 mechanism and Eulerian composition PDF transport used in the reference case. Using the method for determining liftoff height described in [15], there was a difference in liftoff heights of only about four jet diameters between results of the two cases.

The differences in the reported experimental data are likely due to the absolute accuracy of the thermocouples used to measure temperature in the co-flow, which is up to 4% (50–60 K). The Rayleigh measurements of co-flow temperature in the results of [15] for the case with a co-flow temperature nominally 1355 K indicate a mean temperature of 1370 K with an RMS of 25 K. This case was described as having a liftoff height of $35D$. The case from the experimental data of [27] that match this liftoff height has a nominal co-flow temperature of 1405 K (at the same co-flow equivalence ratio as [15] of 0.40)—well within experimental error. The plotted experimental data in [15] appear to deviate to the cooler side of this data point for reasons unexplained in the paper, but still within the boundaries of experimental uncertainty.

The base case for calculations in this paper (marked (a) in Fig. 2) has a co-flow temperature of 1355 K and co-flow velocity of 5.3 m/s. The calculated liftoff height is around 53 diameters. A case with co-flow temperature of 1430 K (marked (b)) is chosen to allow the investigation of a flame with a low liftoff height (28 diameters) and shorter ignition delay times.

Two simple test cases are also used here for validation purposes: (i) a one-dimensional plug flow reactor for simulating autoignition and (ii) a two-dimensional counterflow premixed flame. The plug flow reactor domain is 2 m long and 1 cm wide and is divided into a single row of 1000 equal-sized cells. The counterflow premixed case consists of a 2 × 1-cm domain with a 100 × 50-cell uniform mesh. The premixed flame is stabilized close to the stagnation plane by a counterflow of combustion products at equilibrium composition and the adiabatic flame temperature. Data taken along the symmetry plane are used to simulate a one-dimensional premixed flame. These test cases have been chosen as the simplest reliable examples of their respective flame types. The turbulence length scale affects the width of the flame zone in both cases, but changes in the turbulent kinetic energy do not appreciably affect the ignition delay.

2.3. Boundary conditions

The boundary conditions for the calculations of the turbulent fames and the two test cases are detailed in Table 2. For the turbulent lifted flame cases, boundary conditions in the central fuel jet and the hot co-flow are given. Calculations account for conjugate heat transfer across the steel fuel tube, which is modeled as a steel wall, 0.89 mm thick, with a density of 8030 $kg\,m^{-3}$, a specific heat $C_p = 502.48\ J\,kg^{-1}\,K^{-1}$, and a thermal conductivity of $15.2\ W\,m^{-1}\,K^{-1}$. It is worth noting that the solution

is found to be insensitive to the fuel jet inlet turbulence levels.

The physical submodels and the numerical parameters employed for the test cases are identical to those used in the turbulent lifted flame calculations, except that 100 particles per cell are used in the former, 50 in the latter. For the 1-D autoignition case the initial composition is that of an unburnt mixture fraction of 0.1 from the lifted flame case with a co-flow temperature of 1355 K, corresponding to the conditions just within the ignition zone. For the opposed flow premixed test case, the cold fuel inlet mixture is stoichiometric for a humid methane–air mixture. The counterflow mixture is made up of equilibrium combustion products at the adiabatic flame temperature.

3. Numerical and modeling issues

Mixture fraction for the cases run with the ARM2 mechanism was calculated from the Bilger formulation [28],

$$f = \frac{\frac{2(Y_C - Y_{C,2})}{M_C} + \frac{Y_H - Y_{H,2}}{2M_H} - \frac{Y_O - Y_{O,2}}{M_O}}{\frac{2(Y_{C,1} - Y_{C,2})}{M_C} + \frac{Y_{H,1} - Y_{H,2}}{2M_H} - \frac{Y_{O,1} - Y_{O,2}}{M_O}}. \quad (1)$$

The mass fractions, Y, and elemental masses, M, of carbon, hydrogen, and oxygen, along with the values at the fuel and co-flow inlets (subscripts 1 and 2, respectively) determine the mixture fraction. For the base-case conditions listed in Table 2, the stoichiometric mixture fraction is 0.17. It should, however, be noted that equal diffusivities are assumed in the calculations, and so the mixture fraction based on each element is the same.

3.1. Grid independence

Three grids were tested to determine a mesh resolution to which the numerical solution was independent. The details of the meshes are found in Table 3 and the domain is illustrated in Fig. 3.

Axial and radial profiles of mean and RMS velocity, temperature, and mixture fraction were compared for each of the three meshes, for the base case of $T_{\text{co-flow}} = 1355$ K. Meshes 2 and 3 give close results and either may be used to produce a grid-independent solution. However, the finer mesh (Mesh 3) is selected here and is used in all subsequent calculations.

3.2. ISAT error tolerance

Adequate error tolerances for the ISAT table (ε_{tol}) were determined through investigating the impact of different values on the conditional mean temperature at the stoichiometric mixture fraction, $\langle T|\xi_s\rangle$,

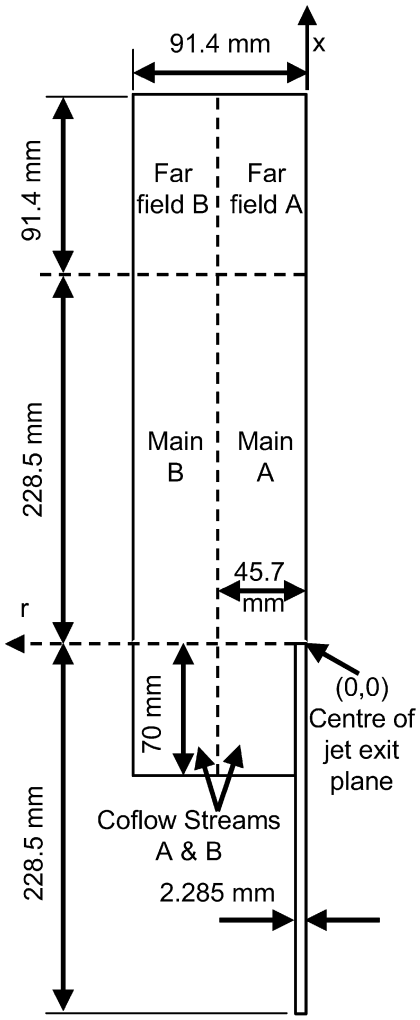

Fig. 3. Diagram of the computational domain.

in the region of $x/D = 10$ to 70 (Fig. 4). With an ODE absolute error tolerance of 1×10^{-8}, ISAT error tolerances of 1×10^{-4}, 2.5×10^{-5}, 6.25×10^{-6}, 1.0×10^{-6}, 2.5×10^{-7}, and 1.0×10^{-7} are tested. The values for which numerically accurate solutions are achieved vary between the mechanisms used here, as detailed in Table 4. Reasons for this variation require an extensive sensitivity analysis which is beyond the scope of this paper. It is worth noting, however, that the ISAT error tolerances set here are refined to achieve high levels of accuracy. The penalty on computational costs is high, but this cost is still below the levels required to perform direct integration.

3.3. Averaging and filtering

The minimum number of particles per cell is determined by choosing an error tolerance around values extrapolated for $N_{\text{PC}} \to \infty$, where the bias would be zero. The base case is calculated with a range of values of $N_{\text{PC}} = 5$, 10, 20, and 50. Values for mean and RMS velocity, temperature, and mixture fraction are plotted against the inverse of N_{PC} in Fig. 5, taken

Table 3
Details of the domain meshes

	x		r		Mesh 1 cells		Mesh 2 cells		Mesh 3 cells	
	From (mm)	To (mm)	From (mm)	To (mm)	X	Y	X	Y	X	Y
Fuel jet	−228.5	0	0	2.285	20	4	40	8	70	15
Co-flow stream A	−70	0	2.285	22.85	10	10	20	20	40	30
Co-flow stream B	−70	0	22.85	91.4	10	10	20	20	40	25
Main domain A	0	228.5	0	22.85	100	14	200	28	300	45
Main domain B	0	228.5	22.85	91.4	100	10	200	20	300	25
Far field domain A	228.5	228.5	0	22.85	10	14	20	28	30	45
Far field domain B	228.5	319.9	22.85	91.4	10	10	20	20	30	25
Total cells					2920		11,680		26,350	

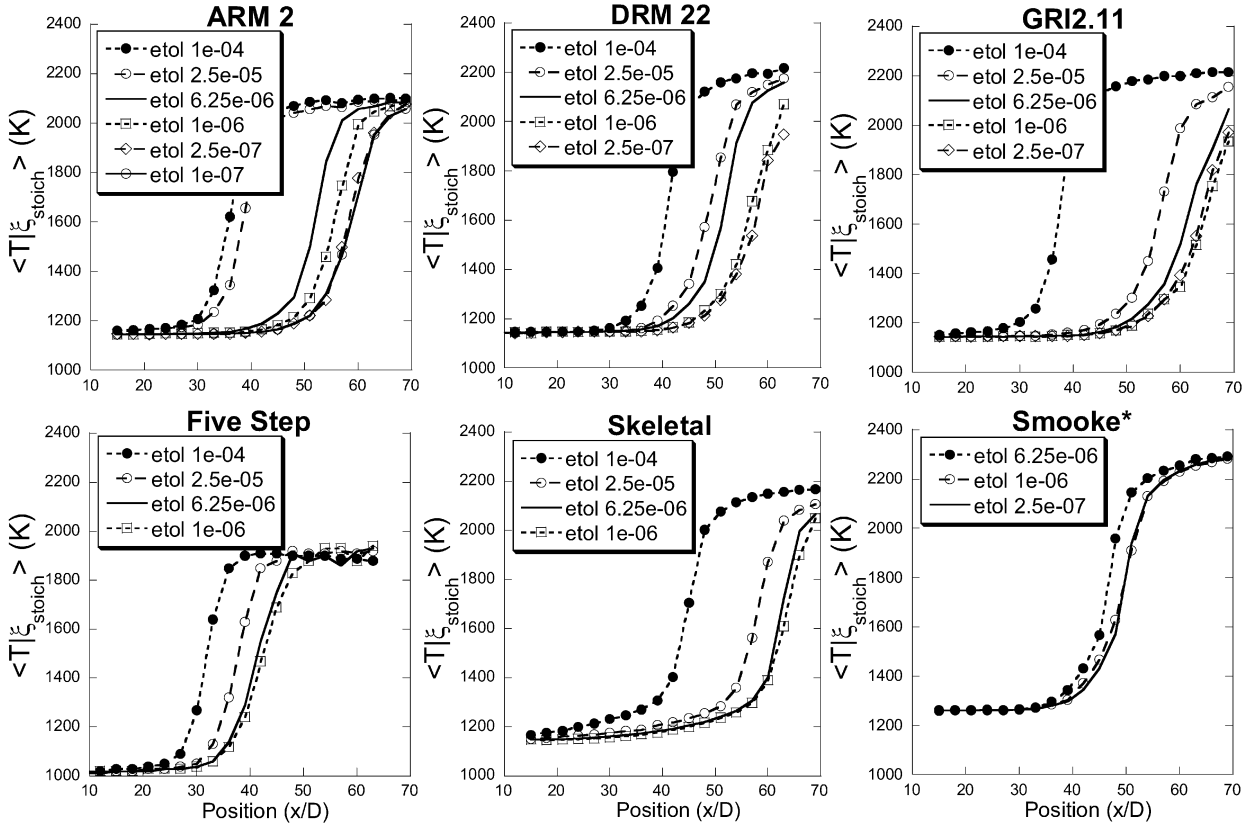

Fig. 4. Mean temperature conditional on stoichiometric mixture fraction versus axial position for the six chemistries investigated: ARM2, DRM22, GRI2.11, Skeletal, 5-step, and Smooke. Data are plotted for calculations at ISAT error tolerances between 1.0×10^{-4} and 1.0×10^{-7}, as indicated. *The Smooke cases were calculated for a flame with $T_{\text{co-flow}} = 1500$ K, due to the longer ignition delay of this mechanism.

Table 4
Numerically accurate values for ISAT error tolerances for each chemical mechanism investigated

Mechanism	ISAT error tolerance
GRI2.11	1.0×10^{-6}
ARM2	2.5×10^{-7}
DRM22	1.0×10^{-6}
Skeletal	6.25×10^{-6}
Smooke	1.0×10^{-6}
5-Step	6.25×10^{-6}

at $x/D = 40$ and $r/D = 2.0$. Taking an error tolerance of ±5%, it is found that the data points lie within this error bar for $N_{\text{PC}} = 20$ or larger. However, a value of $N_{\text{PC}} = 50$ is required to smooth the mean fields sufficiently for the calculation of species transport budgets. A value of $N_{\text{PC}} = 50$ is used in each of the turbulent lifted flames cases, and 100 is used for the test cases. The number of iterations in the pseudo time average, N_{TA}, is set to 1000.

Residual noise in the plots has been attenuated through multiple applications of a 5 × 5 matrix fil-

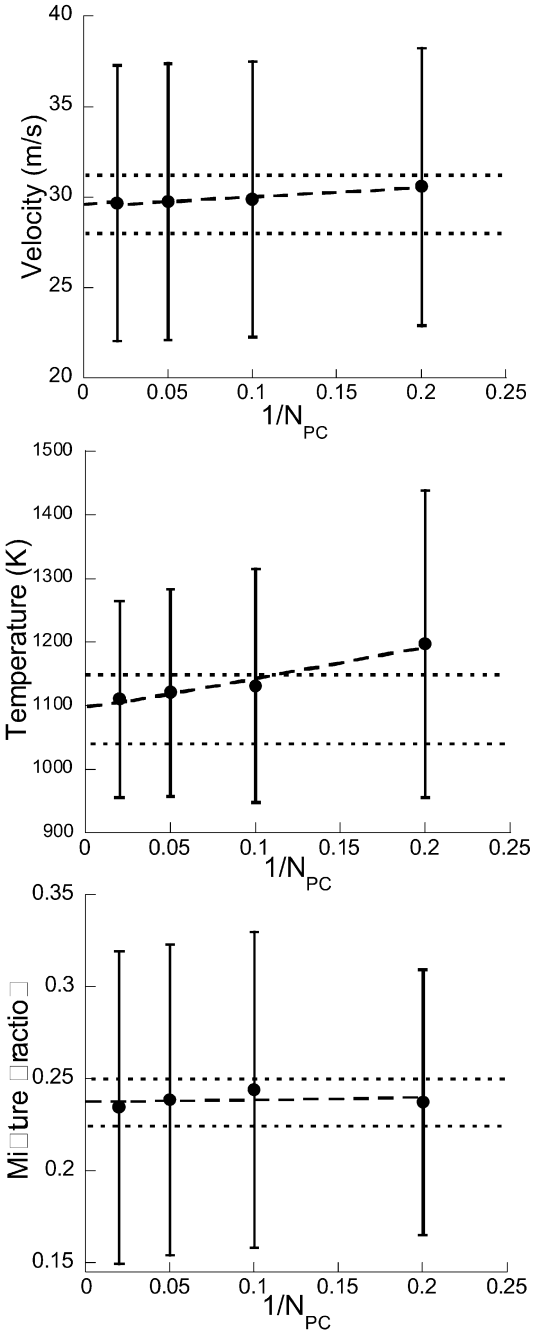

Fig. 5. Richardson regression plots of mean velocity, temperature, and mixture fraction for 5, 10, 20, and 50 particles per cell. X-axis is the inverse of the number of particles per cell. Thick dashed line shows least-squares fit to data. Values with zero bias are taken as the linear extrapolation of this line to zero (i.e., as $N_{\mathrm{PC}} \to \infty$). Horizontal dotted lines indicate $\pm 5\%$ of zero bias value. Error bars indicate ± 1 standard deviation from the data point. Data are taken at $x/D = 40$ and $r/D = 2$.

ter that has been generated from the tensor product of a five-point filter vector $[-3/35,\ 12/35,\ 17/35,\ 12/35,\ -3/35]$ as described in [16]. This is a fourth-order linear filter that minimizes the variance of the filtered function. It has been applied eight times to all the budget results presented in this paper.

3.4. Mixing models

For both the Euclidean minimum spanning trees (EMST) and the modified curl (MC) mixing models, the constant C_ϕ is representative of a molecular mixing time scale. Although controversy still exists about the appropriate value of C_ϕ, earlier research by Pope's group [14,24,29] has found that $C_\phi = 1.5$ is appropriate for EMST, and hence this value is adopted here. For this flow configuration, the EMST model predicts a liftoff height around eight jet diameters lower than that obtained from using modified curl (with $C_\phi = 1.5$) for a co-flow temperature of 1355 K, which is expected due to the localness property of the EMST [14,15].

4. Investigation of the turbulent lifted methane flames

4.1. Radial profiles

Profiles for mean and RMS temperature and mixture fraction at $x/D = 1$ are shown in Fig. 6. It is clear that the calculations near the jet exit plane are well matched to the experimental data.

Radial profiles at axial locations of $x/D = 15$, 30, 40, 50, and 70 are shown for mean and RMS temperature and mixture fraction (Fig. 7), and mean and RMS velocity and OH mass fraction profiles are shown for $x/D = 15$, 30, and 40 in Figs. 8 and 9, respectively. The experimental data at 1355 K co-flow has been compared to the numerical data at 1380 K co-flow. This gives the closest match on OH profiles, which is not surprising given that the measured Rayleigh co-flow temperature for the experimental data is around 1370 K (see Section 2.2), and a 25 K difference in co-flow temperature is well within experimental uncertainty. The velocity profiles of Fig. 8 match remarkably well, especially in the preflame region around $x/D = 30$. This is due to the setting of $C_{\varepsilon 1}$ to 1.6 to compensate for the round-jet/plane-jet anomaly. There is an overprediction of OH at the lean side of the flame, which is probably linked to the slight (around 10%) overprediction of the mixture fraction. This also corresponds to a higher downstream temperature away from the centerline.

4.2. Scatterplots

Scatterplot data of temperature and OH mole fraction versus mixture fraction are presented for a comparison of numerical data taken at $T_{\text{co-flow}} =$ 1380 K to the experimental data (Fig. 10) and for the ARM2 numerical data compared to the full chemistry GRI2.11 calculations (Fig. 11, both taken at 1355 K).

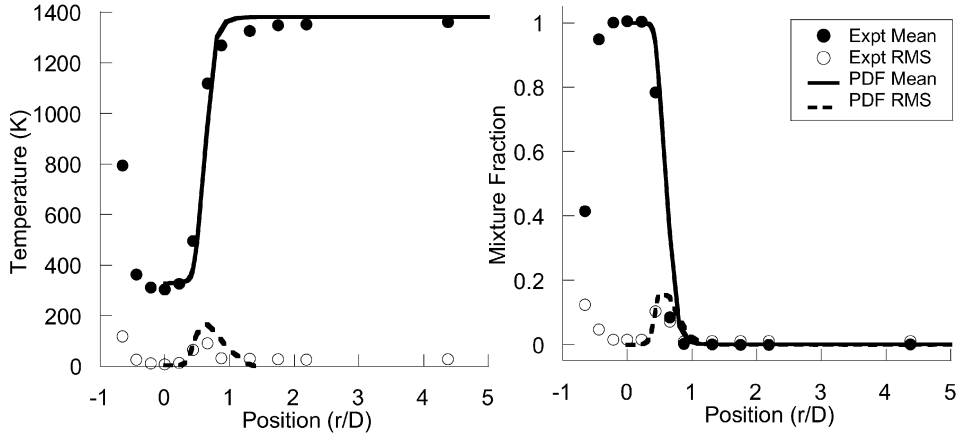

Fig. 6. Numerical and experimental values for mean and RMS temperature and mixture fraction at $x/D = 1$. Numerical data taken from case with $T_{\text{co-flow}} = 1380$ K.

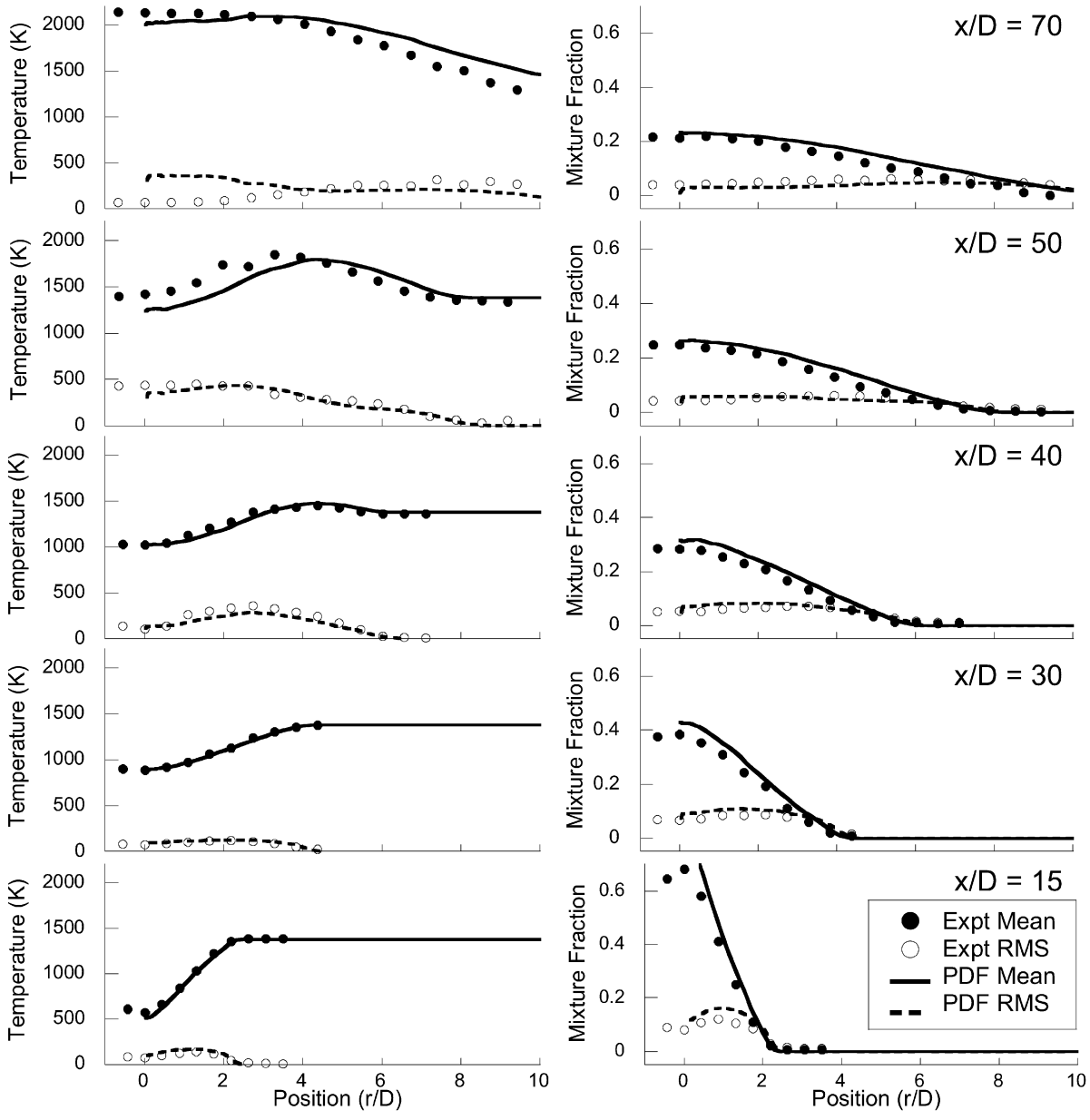

Fig. 7. Radial profiles of mean and RMS temperature and mixture fraction for $T_{\text{co-flow}} = 1380$ K, compared to experimental data of [15].

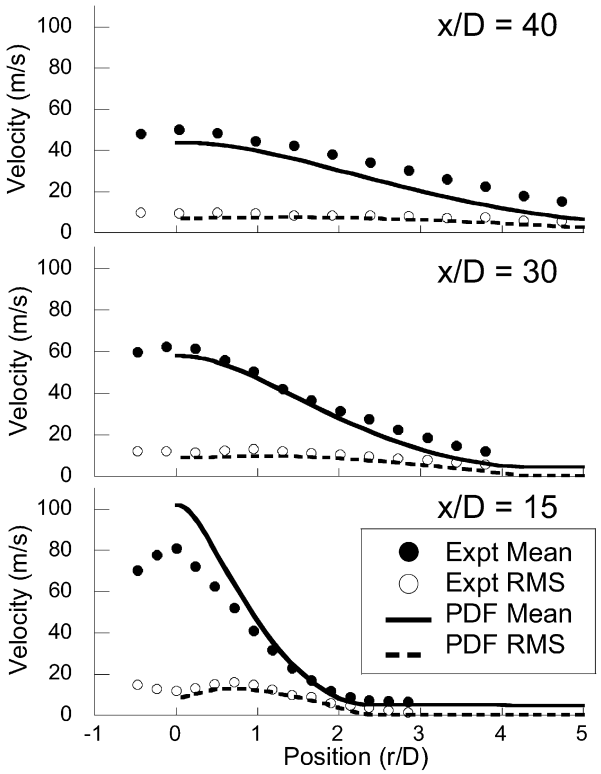

Fig. 8. Radial profiles of mean and RMS velocity for $T_{\text{co-flow}} = 1380$ K, compared to experimental data of [27].

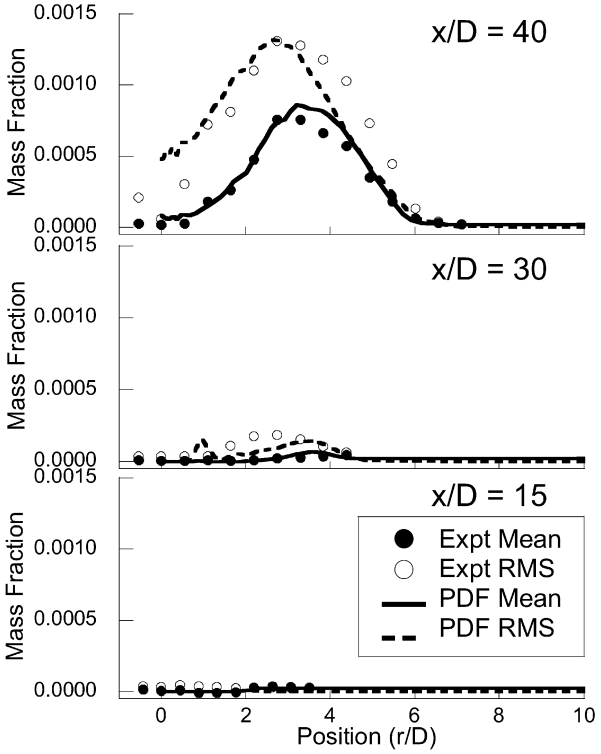

Fig. 9. Mean and RMS OH mass fraction for $T_{\text{co-flow}} = 1380$ K, compared to experimental data of [15].

The bimodal temperature profile is clearly displayed in the calculations. The calculations display a sharper dropoff in temperature on the rich side, which corresponds to a very distinct cutoff in rich mixture OH levels. The peak temperatures and OH production are shifted to the rich side of stoichiometric. Overall, however, the match to the experimental data is quite strong.

To determine if the OH cutoff is an artifact of the mechanism employed, a comparison has been made between ARM2 and GRI2.11 in Fig. 11. The augmented reduced mechanism matches that of the full mechanism well, albeit with a slightly reduced liftoff height.

4.3. Investigation of minor species modeling

The comparison between ARM2 and GRI2.11 is further developed in Fig. 12, where conditional means and RMS of the mass fractions of the ignition precursors CO, CH_2O, CH_3, HO_2, and H_2O_2, as well as OH, are compared at $x/D = 40$ for the cases with $T_{\text{co-flow}} = 1355$ K. Calculations using ARM2 give a liftoff height slightly (around $1D$) lower than those using GRI2.11 mechanism. This results in a slight shift in the peak conditional means toward the stoichiometric mixture fraction and in the higher peak values obtained using ARM2. This is most notable for OH and CO, indicative of the slightly advanced reaction at this location. However, the overall shift is small, and the match in the modeling of the minor species between ARM2 and GRI2.11 is excellent.

5. Results: test cases

The objective of showing results for these test cases is to highlight the differences between the phenomenon of autoignition and that of premixed flame propagation, as these are the two most plausible mechanisms for flame stabilization for the turbulent lifted flames under investigation. These differences may be marked by a buildup of a radical pool prior to ignition or by a different balance of transport processes in the stabilization region. With autoignition, a balance is expected between reaction and convection, while in premixed flame stabilization, the preheat zone is characterized by diffusion balancing convection followed by the reaction zone, where the dominant balance is between reaction and diffusion. These distinctive features may be used to further understand autoignition and to identify its occurrence as opposed to premixed flame stabilization. Further, it is necessary to show that the indicators being examined are capable of distinguishing between the two combustion mechanisms.

The 1-D test case gives an ignition delay of 3 to 3.5×10^{-2} s. This compares to 3.35×10^{-2} s from the full GRI3.0 mechanism, and to predictions

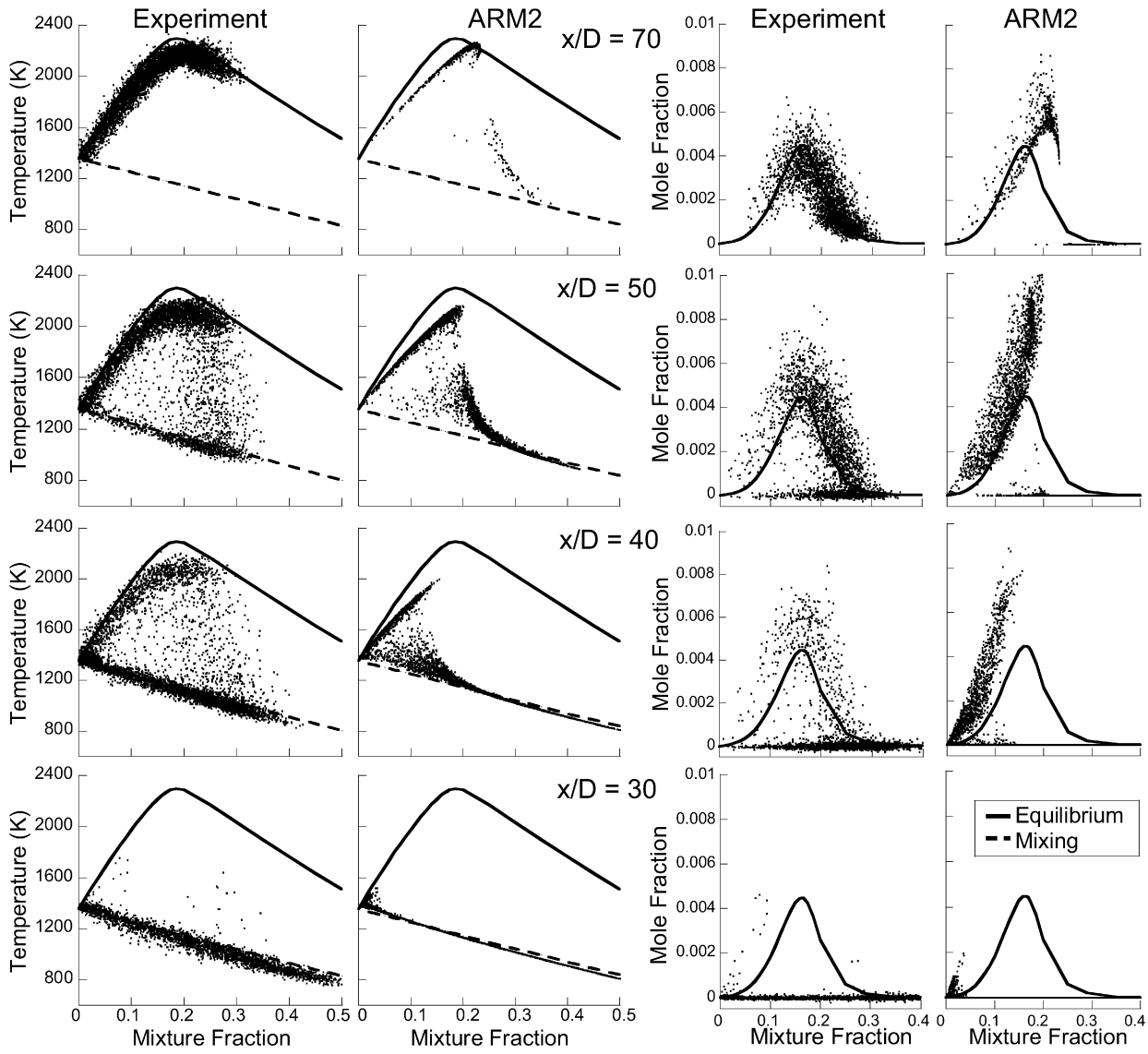

Fig. 10. Scatterplots of temperature (left) and OH mole fraction (right) for $T_{\text{co-flow}} = 1380$ K compared to experimental data of [15]. Pure mixing line (dashed) and adiabatic/equilibrium lines (solid) are shown for reference. Stoichiometric mixture fraction is 0.17.

of 2×10^{-2} s from an empirical relationship based on methane shock tube data [2].

5.1. Build-up of species concentrations

The top two graphs of Fig. 13 show plots versus axial distance for the normalized mean mass fractions of the minor species computed for the autoignition case (LHS) and the premixed flame case (RHS). The peak mass fractions used for normalizing can be found in Table 5. Axial distance through the mean flame is directly related to time, so these plots may be viewed as time histories for species concentrations. Temperature is not shown, as its profiles are similar in shape and location to those of OH.

For the chemical mechanism used here, three principal combustion pathways exist: $CH_3 \rightarrow CH_2O \rightarrow CO$; $C_2H_6 \rightarrow C_2H_4 \rightarrow C_2H_2 \rightarrow CO$; and $HO_2 \rightarrow H_2O_2 \rightarrow 2OH$. For lean mixtures the C_2 pathway is considered to contribute little to the ignition process [5].

In the autoignition case, CH_3, CH_2O, C_2H_2, C_2H_4, C_2H_6, HO_2, CO, and H_2O_2 show an increase in concentration to form a radical pool prior to the runaway of the ignition (the generation of OH). This may be contrasted with the premixed flame case, in which the mass fractions of all the radicals and minor species begin increasing only in the preheat zone, at the same time as the generation of OH. They peak near the axial location of steepest OH gradient (maximum net OH production). These results indicate that the expected buildup of minor species such as CH_2O or HO_2 prior to OH production is a relevant indicator for identifying the occurrence of autoignition, as the minor species in the premixed case all exist concurrently with OH, with no minor species

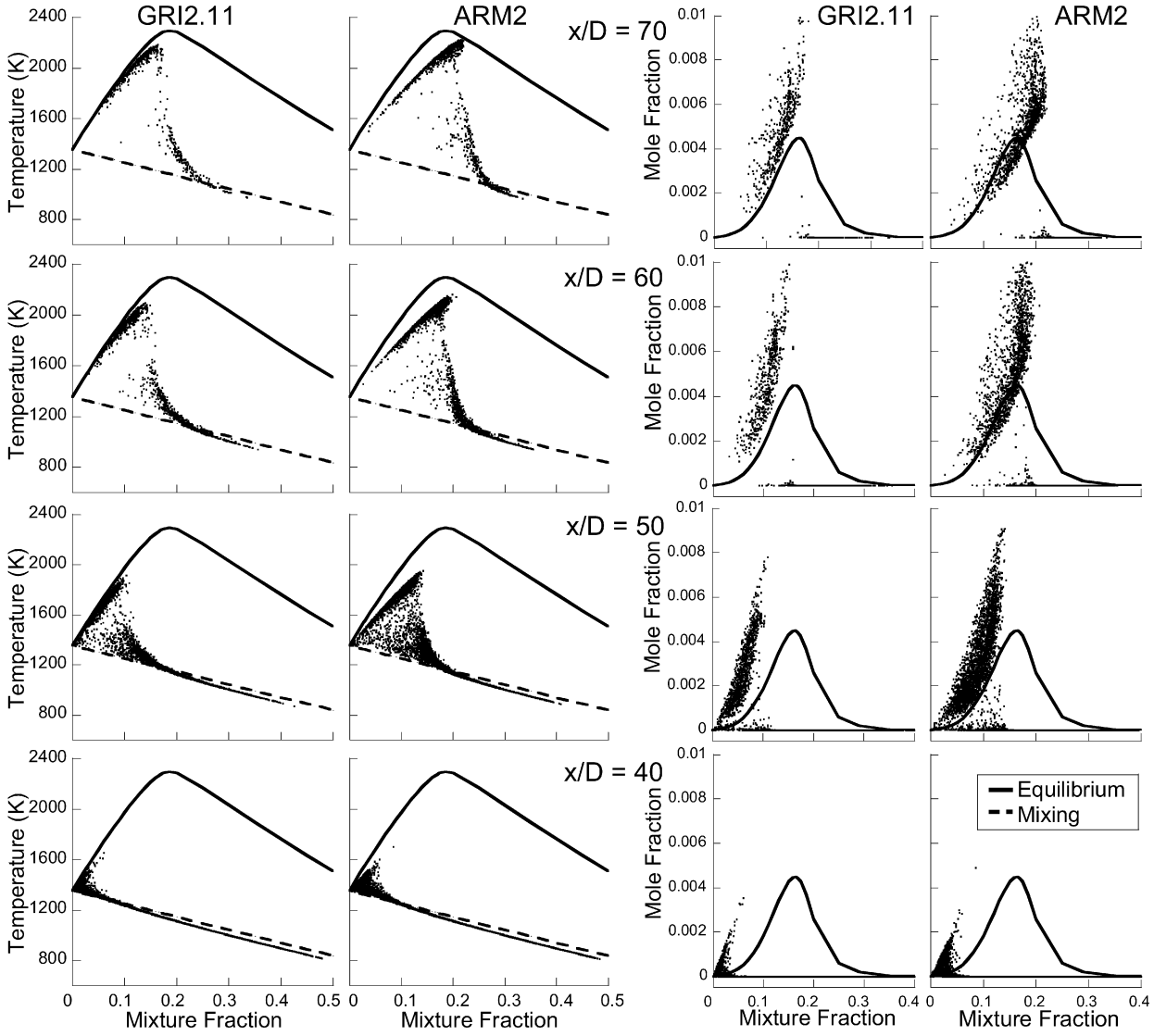

Fig. 11. Scatterplots of temperature (left) and OH mole fraction (right) for $T_{\text{co-flow}} = 1355$ K compared to GRI2.11. Pure mixing line (dashed) and adiabatic/equilibrium lines (solid) are shown for reference. Stoichiometric mixture fraction is 0.17.

exhibiting an increase prior to the onset of OH production.

5.2. *Species transport budgets of convection, diffusion, and reaction (CDR budgets)*

At any point in the domain, the steady-state modeled transport equation (Eq. (2)) for the Favre mean mass fraction of species k is balanced by the three processes of convection, diffusion, and chemical reaction:

$$0 = -\frac{\partial}{\partial x_i}\left(\langle\rho\rangle\tilde{u}_i\tilde{Y}_k\right) + \frac{\partial}{\partial x_i}\left(\frac{\mu_{\text{T}}}{\text{Sc}_{\text{T}}}\frac{\partial\tilde{Y}_k}{\partial x_i}\right) + \langle\rho\rangle\tilde{S}_k. \quad (2)$$

The following points should be noted with respect to the treatment of molecular mixing in the PDF approach and the CDR budgets reported in this paper:

- In the PDF approach, only the molecular mixing contribution of molecular diffusion is considered, since spatial transport due to molecular diffusion is insignificant at high Reynolds numbers. In nonpremixed flames, the rate of molecular mixing is assumed to be determined by the ratio of turbulent dissipation, ε, and kinetic energy, k, independent of the molecular diffusion coefficient. In some PDF studies of premixed flames, the mixing rate is made dependent on the laminar flame speed which in turn depends on molecular diffusion. This approach has been used successfully by both Lindstedt and Vaos [30] and Anand and Pope [31] to calculate the structure of turbulent premixed flames.
- The mixing model adopted here assumes that rate of molecular mixing is determined by the ratio of turbulent dissipation, ε, and turbulent kinetic energy, k, independent of the molecular diffusion coefficient. This is justified because of the high Reynolds numbers of these flows, and be-

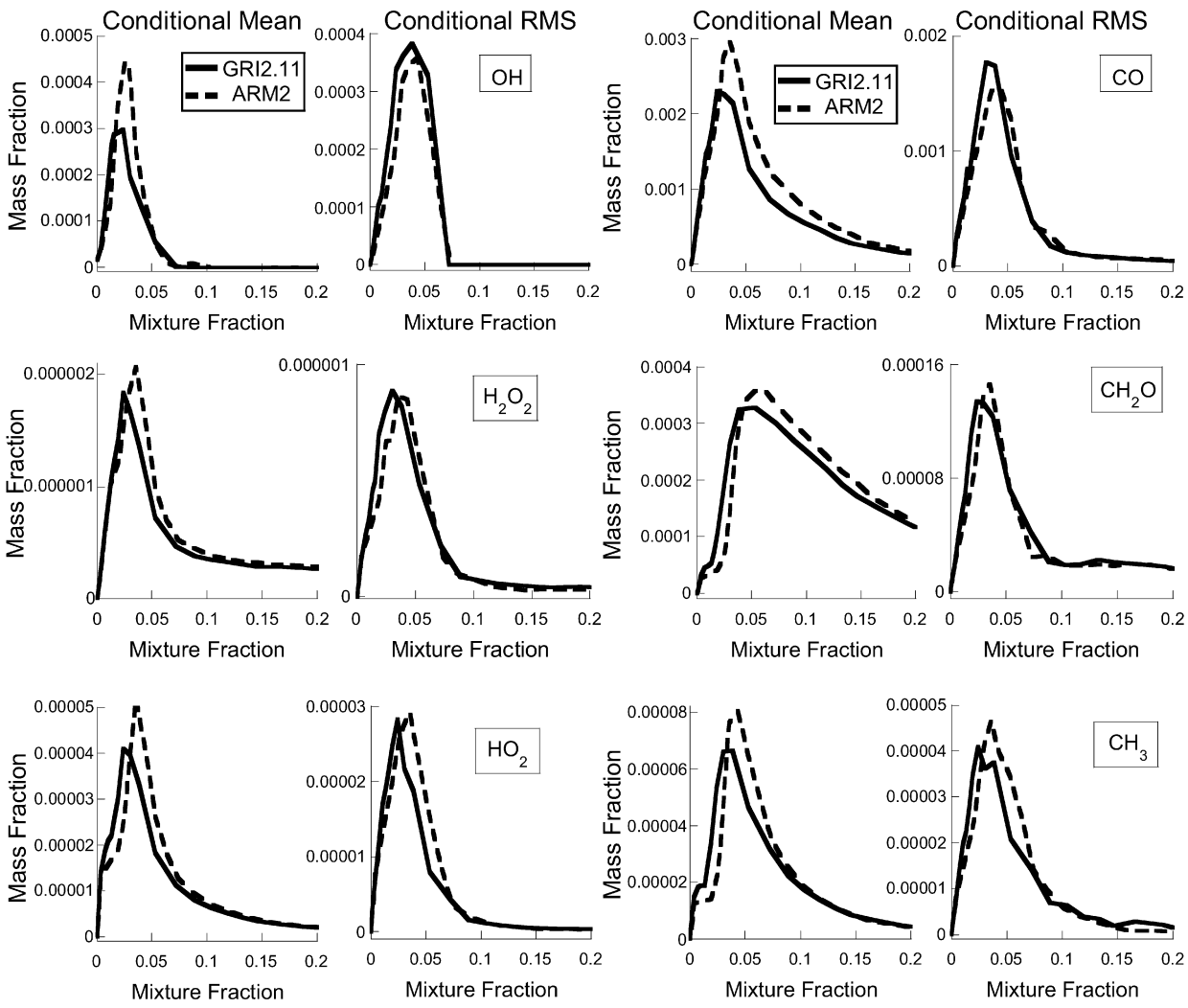

Fig. 12. Conditional mean and RMS of mass fractions of OH and ignition precursor species CH_3, CH_2O, CO, HO_2, and H_2O_2 for $T_{\text{co-flow}} = 1355$ K for ARM2 (open squares) compared to GRI2.11 (solid circles).

cause the strong coupling between the reaction zone and the preheat zone that would prevail in standard premixed flames is not expected here.

- The CDR terms are averaged quantities and hence do not provide any information on the instantaneous structure of the flame. The CDR budgets reported here provide, within the restrictions of the model used, an adequate description of flame stabilization modes and distinguish clearly between the lateral transport of pure fuel and oxidant and axial transport of combustion products.

The first term on the right-hand side of the equation represents convection (C) by the mean flow, the second term is turbulent diffusion (D), and the third is the reaction source term (R). Here, $\langle\rho\rangle$ is the mean density, $\tilde{u}_i$ is the Favre-averaged velocity in the ith direction, $\tilde{Y}_k$ is the Favre-averaged mass fraction of species k, μ_{T} is the turbulent viscosity, Sc_{T} is the turbulent Schmidt number, and $\tilde{S}_k$ is the Favre-averaged chemical source term.

Fig. 13 also shows the CDR budget of CH_2O for the 1-D autoignition case (LHS) and for the 2-D premixed case (RHS) plotted versus distance. The budgets for the autoignition case show, as expected, that the dominant balancing terms are convection and chemical reaction. The diffusion term is an order of magnitude smaller and this is consistent for all of the species. The plots on the RHS that correspond to a premixed flame reveal a preheat zone that exists from $x = 0.004$ to 0.007 m, dominated by a convective–diffusive balance, followed by the reaction zone showing a balance between diffusion and reaction.

The directional components of the diffusion term are calculated separately to allow us to distinguish between axial diffusion, associated with premixed flame propagation, and radial diffusion, which may be present in autoignition stabilization. Each of the calculated budget terms is normalized by a factor of $\rho_{\text{J}} Y_{k,\max}/t_{\text{J}}$, where ρ_{J} is the density of the fuel stream, $Y_{k,\max}$ is the maximum mean species mass fraction for the species k over the whole field, and t_{J}

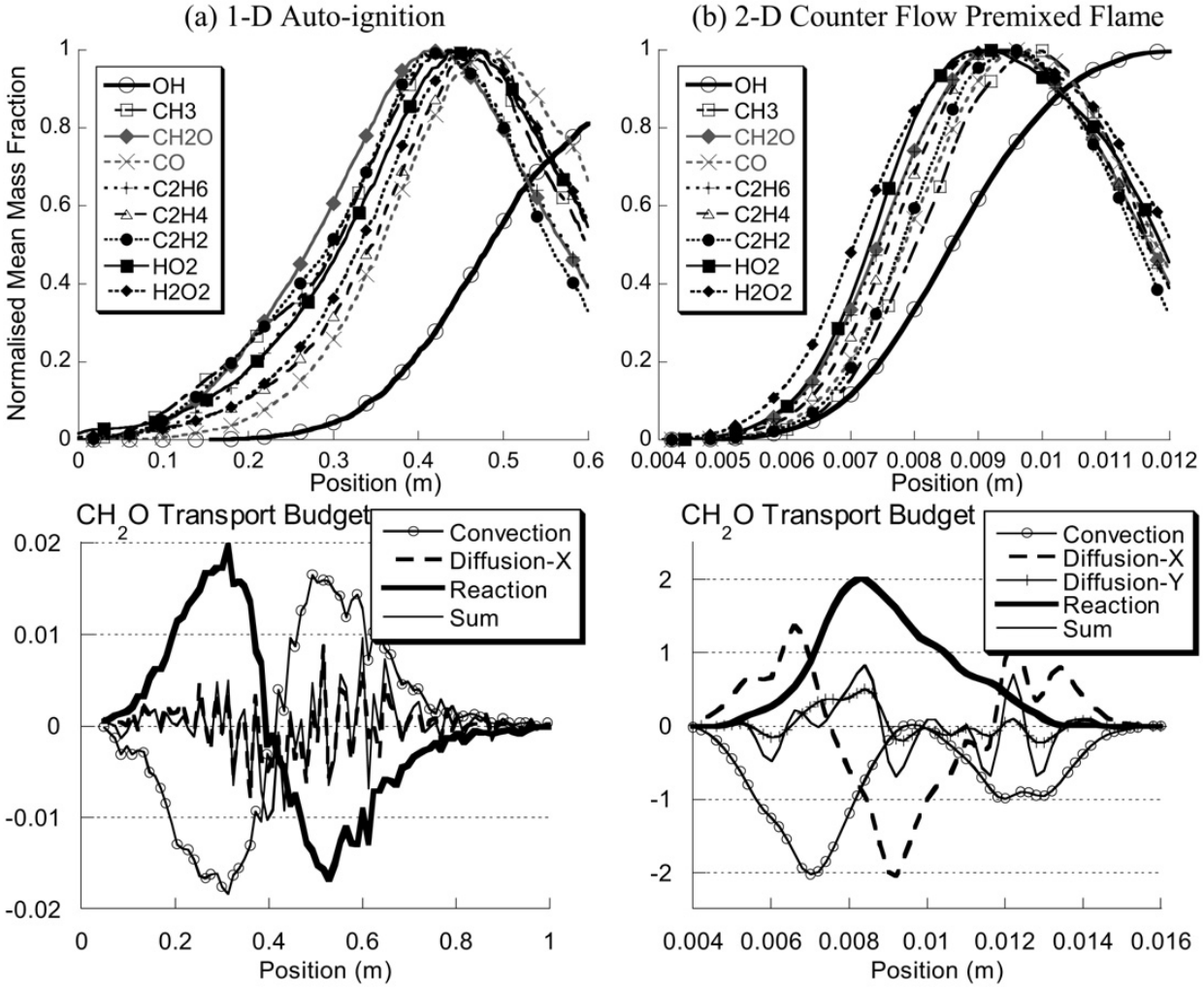

Fig. 13. Normalized mean mass fractions of OH, CH_3, CH_2O, CO, C_2H_6, C_2H_4, C_2H_2, HO_2, and H_2O_2 and species transport budget of CH_2O for (a) 1-D autoignition along the centerline of the domain and (b) 2-D counterflow premixed flame along the symmetry plane.

Table 5
Peak mass fractions in test cases

Species	Peak mass fractions	
	1-D autoignition	2-D premixed
OH	1.3×10^{-3}	9.7×10^{-4}
CH_3	2.0×10^{-5}	5.9×10^{-6}
CH_2O	4.2×10^{-4}	6.8×10^{-5}
CO	1.0×10^{-3}	4.3×10^{-3}
C_2H_6	3.4×10^{-4}	8.7×10^{-5}
C_2H_4	2.0×10^{-4}	5.3×10^{-5}
C_2H_2	5.7×10^{-6}	5.2×10^{-6}
HO_2	1.4×10^{-5}	5.4×10^{-6}
H_2O_2	1.1×10^{-6}	2.5×10^{-6}

is a representative time scale for the fuel flow. For the lifted flame cases, t_J is taken to be the jet diameter divided by the fuel bulk velocity; for the plug flow reactor, the domain width divided by the inlet velocity; and for the premixed counterflow burner, twice the inlet width divided by the inlet velocity. The values of these factors are reported in Table 6.

Table 6
Normalizing factors $\rho_J Y_{k,\max}/t_J$ for CDR budgets

Case	Normalizing factor (kg/m^3 s)			
	CH_4	CO_2	CO	CH_2O
1-D autoignition	–	–	–	0.396
2-D premixed	–	–	–	0.002
Lifted flame, $T_{\text{co-flow}} = 1355$ K	1302.2	1124.5	58.89	5.223
Lifted flame, $T_{\text{co-flow}} = 1430$ K	1686.2	1484.5	82.5	7.643

One of the key tests for the accuracy of the budget terms for each species is how close the sum of the terms is to zero. This sum is plotted on all budget graphs. Because the calculations achieve a statistically stationary state, it follows that the CDR budget as implicitly evaluated in the particle method is in balance. Presumably, therefore, any observed imbalance

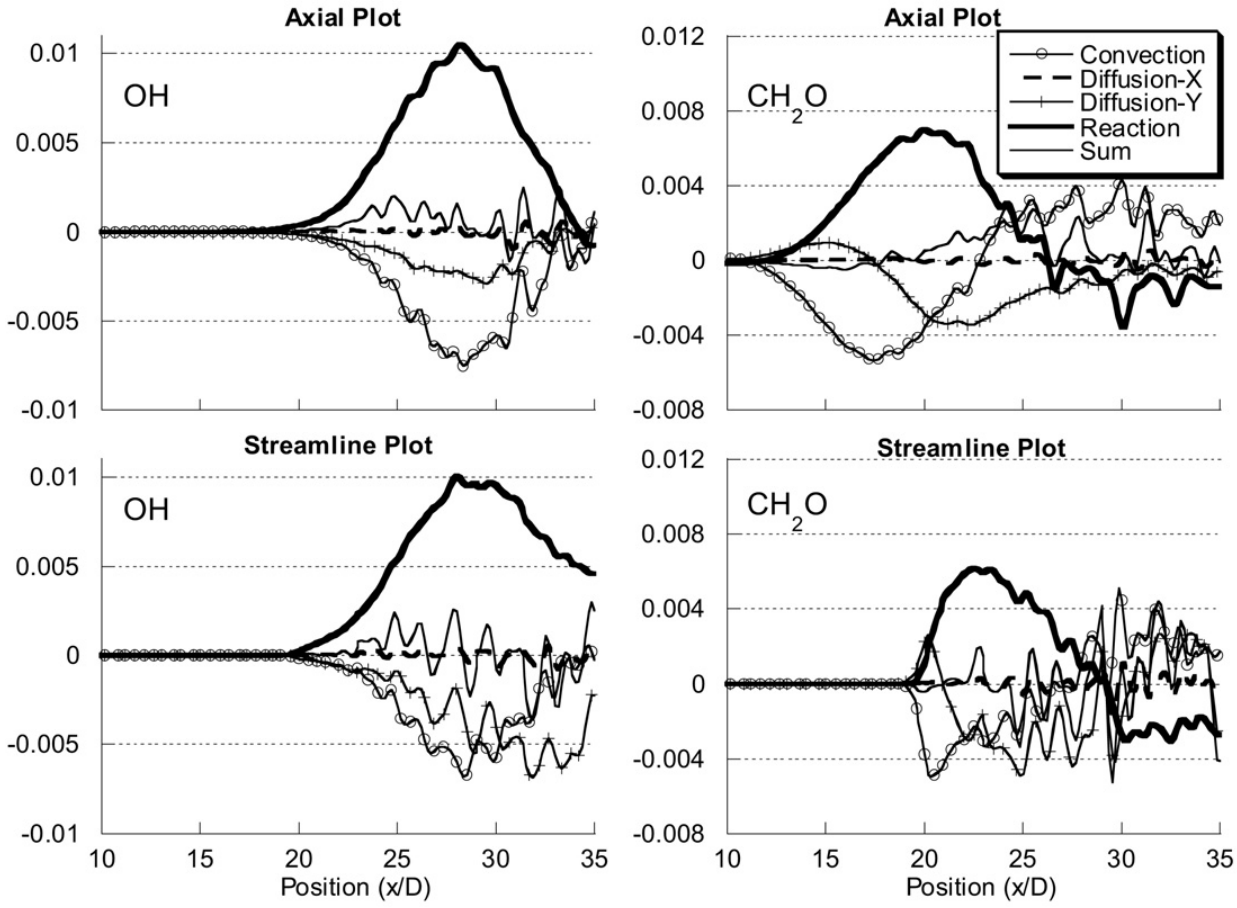

Fig. 14. Species transport budget plots along stream line and axial line for OH and CH_2O for case $T_{\text{co-flow}} = 1430$ K.

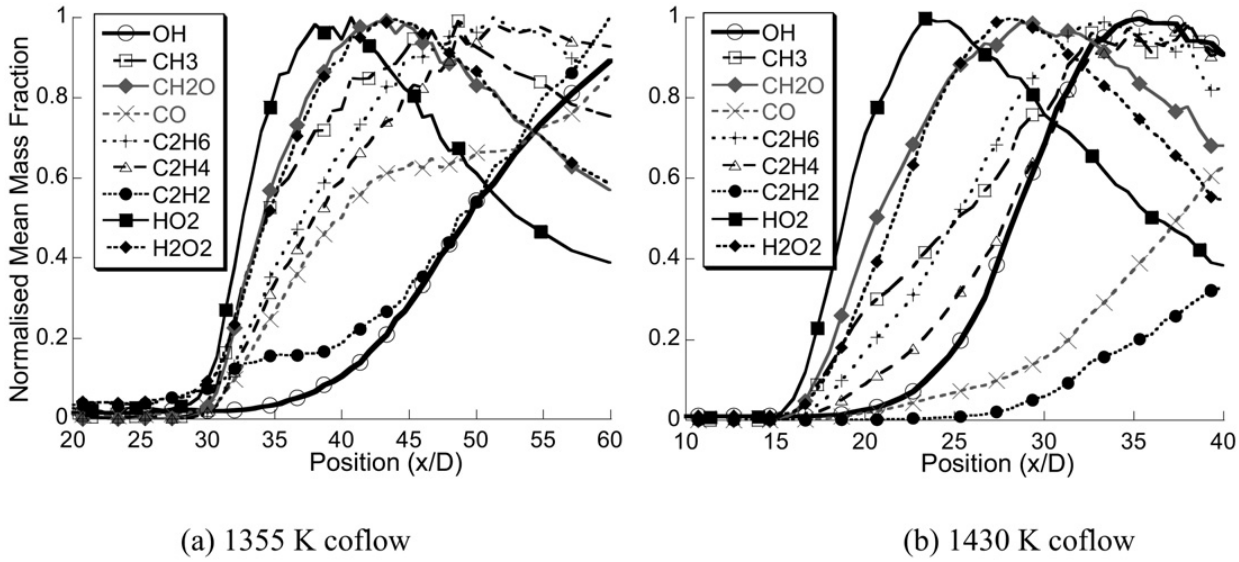

Fig. 15. Axial profiles of normalized mean mass fractions of OH, CH_3, CH_2O, CO, C_2H_6, C_2H_4, C_2H_2, HO_2, and H_2O_2 for lifted flames with co-flow temperatures of (a) 1355 K and (b) 1430 K. Profiles are taken along an axial line passing through the mean flame base at $r/D = 4.5$ for (a) and $r/D = 2.5$ for (b).

arises because the three contributions presented in the figures have been evaluated differently than in the particle method. Specifically, any imbalance may be due to splitting errors and spatial discretization errors in addition to statistical fluctuations. Further, the symmetry line of the 2-D premixed case approximates a 1-D flow: therefore there should be almost no lateral diffusion, so the observed values here for 'Diffusion-Y' are another indicator of the level of uncertainty in the calculations.

6. Results: turbulent lifted flames

The autoignition indicators discussed earlier are applied here to two selected turbulent flames with a fuel jet velocity of 100 $\mathrm{m\,s^{-1}}$ and different co-flow temperatures, $T_{\text{co-flow}} = 1355$ and 1430 K. These flames correspond to high ($53D$) and low ($28D$) liftoff heights and are marked by (a) and (b) in Fig. 2.

The liftoff height is determined by first defining an axial line that starts at the jet exit plane and intersects the most upstream location of the contour of mean mass fraction of OH $= 5 \times 10^{-5}$. This threshold value for OH is selected so that it is well above the OH levels encountered in the co-flow. The liftoff height is then defined at the location along this axial line where the axial gradient of OH reaches a maximum. All axial profiles shown hereon are plotted along the line defined above: $r = 4.5D$ for case (a) and $r = 2.5D$ for case (b).

It is worth noting here that plots along a mean streamline may be more representative of the time history of a fluid parcel than an axial plot at a fixed radial location. However, the latter is used to facilitate the reporting of axial and radial terms for diffusion and to enable the accurate implementation of the smoothing algorithm. Both methods of reporting the data yield the same conclusions, as seen from the species transport budget shown in Fig. 14 for OH and CH_2O for the $T_{\text{co-flow}} = 1430$ K case. In this region of interest, the mean streamline lies almost parallel to the axis and there is little discernible difference for the OH budget. The information contained in the upstream portion of the formaldehyde plot ($x/D = 15$–20) is compressed in the streamline plot; however, the key features are still present, in that the peak generation of CH_2O still precedes the production of OH, and is itself preceded by a region of convective–radial diffusive balance.

6.1. Buildup of species concentrations

Axial profiles of the normalized mass fractions of the precursor species and OH are plotted through the stabilization points in Fig. 15 for the two flames studied here. The peak mass fractions for both cases are detailed in Table 7. It is interesting to note the significantly higher concentrations of CH_3, CO, and C_2H_2 in the higher co-flow temperature case. For case (a), with $T_{\text{co-flow}} = 1355$ K, the concentrations of CO, CH_2O, CH_3, C_2H_6, C_2H_4, C_2H_2, H_2O_2, and HO_2 start to increase at about $x/D = 30$, before the onset of hydroxyl radical at about $x/D = 38$. This is fully consistent with the test case describing autoignition, implying that this is the dominant stabilization mechanism in this flame.

Table 7
Peak mass fractions in lifted flame cases

Species	Peak mass fractions	
	(a) 1355 K co-flow	(b) 1430 K co-flow
OH	2.7×10^{-3}	3.1×10^{-3}
CH_3	3.8×10^{-5}	1.1×10^{-4}
CH_2O	2.3×10^{-4}	3.1×10^{-4}
CO	3.1×10^{-3}	3.1×10^{-2}
C_2H_6	2.2×10^{-4}	5.1×10^{-4}
C_2H_4	1.4×10^{-4}	3.9×10^{-4}
C_2H_2	1.0×10^{-5}	3.5×10^{-4}
HO_2	1.9×10^{-5}	1.8×10^{-5}
H_2O_2	1.2×10^{-6}	1.3×10^{-6}

Both CO and C_2H_2 exhibit a pattern of production upstream of the autoignition zone to a plateau, followed by accelerated production within the stabilization region. The C_2H_2 pattern is not replicated in the full GRI2.11 mechanism results, so it must be an artifact of the ARM2 mechanism; however, the CO pattern is consistent in the GRI2.11 mechanism.

For case (b) with $T_{\text{co-flow}} = 1430$ K, the concentrations of CH_3, CH_2O, C_2H_6, C_2H_4, H_2O_2, and HO_2 all start to build up at $x/D = 15$, well before OH ($x/D = 22$). CO and C_2H_2 are not generated in significant quantities until deep into the flame, however. While this behavior is not fully consistent with the autoignition test case presented earlier, it is also not indicative of premixed flame stabilization.

In both cases, the presence of CH_2O as a distinct precursor to the flame front may be of use to experimentalists, as this species is present in significant quantities and is relatively easy to image using laser-induced fluorescence. The GRI2.11 mechanism confirms the buildup of formaldehyde prior to the flame front.

6.2. CDR budgets

Fig. 16 shows axial profiles of convection, reaction, and diffusion terms for CH_4, CO_2, OH, and CH_2O calculated through the stabilization points for both flames. Due to the formulation of Eq. (2), negative convection indicates an increasing flux of $\langle\rho\rangle\tilde{u}_i\tilde{Y}_k$. The CDR budgets plotted in Fig. 16 are intentionally selected to enable the comparison of (i) a major species that is convected in one of the inlet streams (CH_4); (ii) a major species that exists solely as a reaction product (CO_2); (iii) a principal combustion radical (OH); and (iv) an ignition precursor (CH_2O).

The onset of mixing of the two streams is clearly delineated in the CH_4 and CH_2O plots. In both flame cases, the fuel stream mixes for around 5 diameters

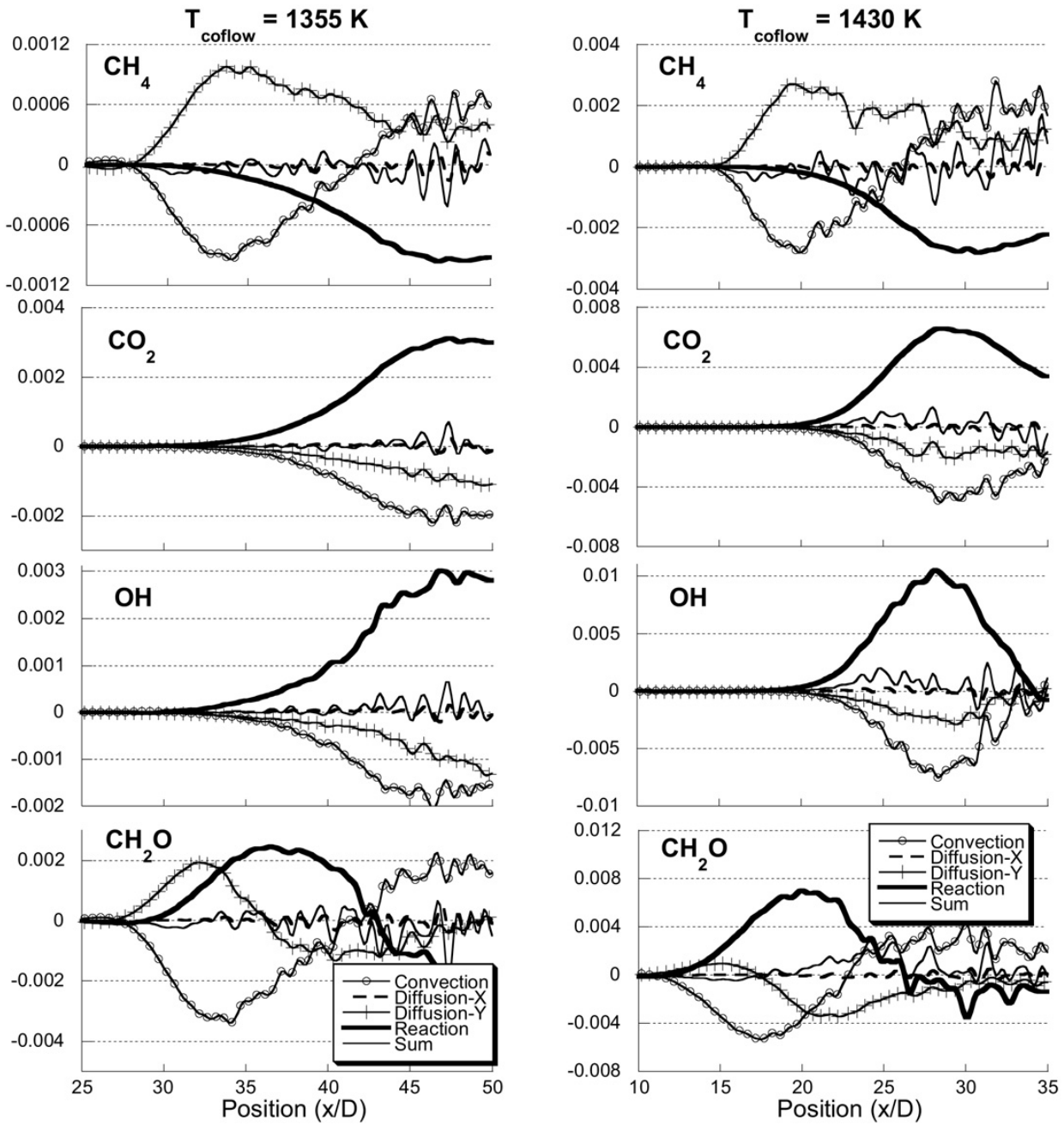

Fig. 16. Species transport budgets of CH_4, CO_2, OH, and CH_2O for lifted flames with co-flow temperatures of (a) 1355 K and (b) 1430 K. Profiles are taken along an axial line passing through the mean flame base at $r/D = 4.5$ for (a) and $r/D = 2.5$ for (b).

prior to the onset of fuel consumption. The formaldehyde radical is formed very early in the flow upstream and closer to the axis than its first occurrence along the plotted axial line. Along the plot line, this leads to a convective–diffusive balance even upstream of the initiation of significant reaction.

The production of OH and CO_2 occur in a location similar to that of CH_4 consumption, and with these species the mode of combustion is clearest of all—negligible axial diffusion, with reaction balanced principally by convection, with some minor radial diffusion. Note that in all four species transport budgets for both flame cases, axial diffusion is negligible at all times, confirming that these flames are being calculated as stabilized through autoignition.

It is evident from the results presented here that the CDR budget is indeed a good marker for the occurrence of autoignition. The buildup of a radical pool in the preignition zone is a less rigorous indicator but useful for studying the role of precursors in autoignition. Carbon monoxide is observed to play an important role both as an ignition precursor and as a principal combustion product. While present in relatively small mass fractions, species such as HO_2 and H_2O_2 still appear to play an important role in the autoignition of methane. Formaldehyde (CH_2O) stands

out as a consistent precursor species regardless of flame chemistry and liftoff height.

7. Conclusions

The hybrid PDF-RANS method is used here with detailed chemistry to compute the species concentrations and their transport budgets of convection, diffusion, and reaction (CDR) in turbulent lifted flames of methane issuing in vitiated co-flows. Several chemical mechanisms are tested and results for the ARM2 mechanism compare favorably with both experimental results and the GRI2.11 mechanism. Test cases representing autoignition and premixed flame stabilization are developed as platforms for identifying the occurrence of autoignition and premixed flame propagation, as these are the two most likely stabilization mechanisms in the turbulent lifted flame cases. The CDR budgets show clearly that the turbulent lifted flames are stabilized by autoignition, whereas if only the buildup of radical species is used as a marker, the results for the high-co-flow temperature cases would be less conclusive, due to CO being absent from the radical pool. It is therefore concluded that the CDR budget is a very useful numerical marker for identifying the occurrence of autoignition, characterized by a balance between convection and reaction, with little or no axial diffusion through the flame stabilization region.

Acknowledgments

This work is supported by the Australian Research Council and the US Air Force Office of Scientific Research Grant No. F49620-00-1-0171. Aspects of this research were conducted using the resources of the Cornell Theory Center, which receives funding from Cornell University, New York State, federal agencies, foundations, and corporate partners.

References

[1] A.H. Lefebvre, Gas Turbine Combustion, Taylor and Francis, Philadelphia, PA, 1998, pp. 57–62.
[2] L.J. Spadaccini, M.B. Colket III, Prog. Energy Combust. Sci. 20 (1994) 431–460.
[3] C. Safta, C.K. Madnia, Combust. Flame 144 (2005) 64–73.
[4] R. Seiser, K. Seshadri, Proc. Combust. Inst. 30 (2005) 407–414.
[5] S.C. Li, F.A. Williams, J. Eng. Gas Turbines Power 124 (2002) 471–480.
[6] J. Huang, P.G. Hill, W.K. Bushe, S.R. Munshi, Combust. Flame 136 (2004) 25–42.
[7] E. Mastorakos, T.A. Baritaud, T.J. Poinsot, Combust. Flame 109 (1997) 198–223.
[8] H. Sreedhara, K.N. Lakshmisha, Proc. Combust. Inst. 29 (2002) 2069–2077.
[9] R. Hilbert, D. Thévenin, Combust. Flame 128 (2002) 22–37.
[10] T. Echekki, J.H. Chen, Combust. Flame 134 (2003) 169–191.
[11] R. Cabra, http://www.me.berkeley.edu/cal/VCB/Data/VCMAData.html.
[12] http://www.aeromech.usyd.edu.au/thermofluids/.
[13] A.R. Masri, R. Cao, S.B. Pope, G.M. Goldin, Combust. Theory Model. 8 (2004) 1–22.
[14] R. Cao, S.B. Pope, A.R. Masri, Combust. Flame 142 (2005) 438–453.
[15] R. Cabra, J.Y. Chen, R.W. Dibble, A.N. Karpetis, R.S. Barlow, Combust. Flame 143 (4) (2005) 491–506.
[16] R.L. Gordon, A.R. Masri, S.B. Pope, G.M. Goldin, Combust. Theory Model. 11 (3) (2007) 351–376.
[17] J. de Charentenay, D. Thévenin, R. Hilbert, in: Proceedings of the European Combustion Meeting ECM03, Orléans (France), 2003, pp. 132/1–132/6.
[18] C.J. Sung, C.K. Law, J.Y. Chen, Combust. Flame 125 (2001) 906–919.
[19] S.B. Pope, Combust. Theory Model. 1 (1997) 41–63.
[20] GRI-Mech web site, http://www.me.berkeley.edu/grimech.
[21] DRM web site, http://www.me.berkeley.edu/drm/.
[22] S. James, M.S. Anand, M.K. Razdan, S.B. Pope, J. Eng. Gas Turbines Power Trans. ASME 123 (2001) 747–756.
[23] M.D. Smooke, I.K. Puri, K. Seshadri, Proc. Combust. Inst. 21 (1986) 1783–1792.
[24] R. Cao, S.B. Pope, Combust. Flame 143 (2005) 450–470.
[25] H.P. Mallampalli, T.H. Fletcher, J.Y. Chen, Paper 96F-098, presented at the Fall Meeting of the Western States Section of the Combustion Institute, University of Southern California, Los Angeles, CA, October 28–29, 1996.
[26] R. Cabra, T. Myrvold, J.Y. Chen, R.W. Dibble, A.N. Karpetis, R.S. Barlow, Proc. Combust. Inst. 29 (2002) 1881–1888.
[27] R.L. Gordon, S.H. Stårner, A.R. Masri, R.W. Bilger, in: 5th Asia–Pacific Conference on Combustion, Adelaide, Australia, 18–20 July 2005, pp. 333–336.
[28] R.W. Bilger, S.H. Stårner, R.J. Kee, Combust. Flame 80 (1990) 135–149.
[29] J. Xu, S.B. Pope, Combust. Flame 123 (3) (2000) 281–307.
[30] R.P. Lindstedt, E.M. Vaos, Combust. Flame 145 (2006) 495–511.
[31] M.S. Anand, S.B. Pope, Combust. Flame 67 (1987) 127–142.